Lead-free high-entropy $Ba(Ti_{0.2}Zr_{0.2}Hf_{0.2}Sn_{0.2}Ce_{0.2})O_3$ ceramics: Structural stabilisation and impedance spectroscopic insights for high-temperature electronic applications

Rupesh Kumar[1], Raj Kumar Singh[1], Kumari Mamta[2], Sumit Kumar Roy[3], Sushil Kumar Pandey[4,*]

[1]*University Department of Physics, Ranchi University, Ranchi-834008, India*

[2]*Dept. of Physics, Nalanda College of Engineering, Chandi, Nalanda-803108, India*

[3]*Department of Physics, St. Xavier's College, Ranchi University, Ranchi-834001, India*

[4]*Department of Chemistry, St. Xavier's College, Ranchi University, Ranchi-834001, India*

Received 21 December 2025; received in revised form 3 March 2026; accepted 20 March 2026

Abstract

A novel high-entropy perovskite, $Ba(Ti_{0.2}Zr_{0.2}Hf_{0.2}Sn_{0.2}Ce_{0.2})O_3$, was successfully synthesized through a conventional solid-state reaction route and finally sintered at 1350 °C for 12 h. Powder X-ray diffraction and Rietveld refinement confirmed the formation of a single-phase cubic structure with space group Pm-3m. Scanning electron microscopy coupled with EDX mapping revealed an uniform microstructure and homogeneous elemental distribution. The electrical properties were investigated using impedance spectroscopy over a temperature range of 35 to 495 °C and a frequency range of 100 Hz to 1 MHz. The real part of impedance decreased with increasing temperature, indicating negative temperature coefficient of resistance (NTCR) behaviour. The imaginary impedance and electrical modulus spectra exhibited temperature-dependent relaxation with peak shifting toward higher frequencies, confirming thermally activated charge transport. The Nyquist plot analysis revealed separate contributions from grains and grain boundaries, demonstrating mixed bulk and interfacial conduction mechanisms. These results establish $Ba(Ti_{0.2}Zr_{0.2}Hf_{0.2}Sn_{0.2}Ce_{0.2})O_3$ as a promising candidate for high-temperature electronic and sensing applications.

***Keywords**: high-entropy, perovskite oxide, impedance spectroscopy, relaxation behaviour, thermal stability*

I. Introduction

Perovskites are a class of oxides renowned for their unique and versatile properties. These materials adhere to the general formula ABO_3, where A^{2+} and B^{4+} represent the appropriate cations. Perovskite oxides are distinguished by a unique crystal structure comprising three distinct sublattices: i) A-cation sublattice coordinated by twelve oxygen atoms, ii) B-cation sublattice coordinated by six oxygen atoms and iii) network of oxygen anions arranged in octahedral geometry. In 1926, Goldschmidt introduced the concept of the tolerance factor (t), which is used to assess the stability of perovskite structures [1]. This factor is determined using the ionic radii of the A cation R_A, the B cation R_B and the oxygen anion R_O according to the formula:

$$t = \frac{R_A + R_O}{\sqrt{2}\left(R_B + R_O\right)} \quad (1)$$

Stability in cubic perovskites is typically achieved when the tolerance factor (t) falls between 0.9 and 1. Values above 1 often lead to the formation of hexagonal or tetragonal phases, while values below 0.9 can induce orthorhombic or rhombohedral phases [2]. ABO_3 perovskite oxides are notable for their exceptional range of excellent physical properties (such as dielectric, ferroelectric and multiferroic properties), which make them suitable for a wide array of applications. These materials are used as thermal barrier coatings, irradiation-resistant components, proton conductors and energy conversion and storage technologies [3–7], as well in solid oxide fuel cells, photocatalysis and microelectronics [8–16]. This

*Corresponding author: tel: +91 9534074699
e-mail: *sushilsxc@gmail.com*

remarkable versatility highlights their significance in numerous advanced technological domains.

High-entropy perovskites (HEPs) are stabilised by configurational entropy due to the random distribution of multiple cations on a single lattice site. This characteristic distinguishes them from traditional solid-state solutions and makes their properties difficult to predict, offering potential opportunities for discovering new functionalities. The unique nature of such materials has led to the development of exceptional properties with applications in electronics, energy storage, nuclear waste management and high-temperature materials [17–23]. The first high entropy perovskite was confirmed in 2017 by Jiang *et al*. [24], sparking significant interest in this field.

In this article we have successfully synthesised a new high entropy perovskite namely $Ba(Ti_{0.2}Zr_{0.2}Hf_{0.2}Sn_{0.2}Ce_{0.2})O_3$. Initial structural characterisation and electrical measurements were carried out and discussed below.

II. Experimental

In this study, the solid-state synthesis method was employed to prepare the samples using high-purity precursors: $BaCO_3$ (99.8%, Fisher Scientific), ZrO_2 (99%, Sigma Aldrich), HfO_2(99.99%, Nano Shel), TiO_2 (99.9%, Thermo Scientific), SnO_2 (99.9%, Sigma Aldrich) and CeO_2 (99.9%, Alfa Aesar). The precursors were mixed in stoichiometric proportions and manually ground in a mortar and pestle for 2 h to ensure uniformity. The resulting powder was then pressed into pellets with a 10 mm diameter using a hydraulic press at pressure of 5 tons. The pellets underwent an initial calcination at 1300 °C for 12 h, followed by intermediate grinding for 2 h. The obtained powder was uniaxially pressed at 5 tons into pellets with a 10 mm diameter and finally sintered at 1350 °C for 12 h to improve structural integrity.

Powder X-ray diffraction (PXRD) and phase analyses of the calcined and sintered samples were performed using a Rigaku Mini flex 600 and Full Prof Suite software, respectively. The elemental composition and chemical uniformity were examined through scanning electron microscopy (SEM) with energy dispersive spectroscopy (EDS) on a ZEISS Sigma 500 VP SEM system. To characterise the electrical properties, measurements were conducted over a temperature range of 35 to 495°C and a frequency range of 100 Hz to 1 MHz using A DPI-1100 microprocessor-controlled temperature controller (Sartech Intl., India) and a HIOKI 3532-50 LCR meter (Japan). To facilitate these measurements, conducting silver paste (99.9%, Nano Shel) was applied to both sides of the samples, converting them into parallel plate capacitors.

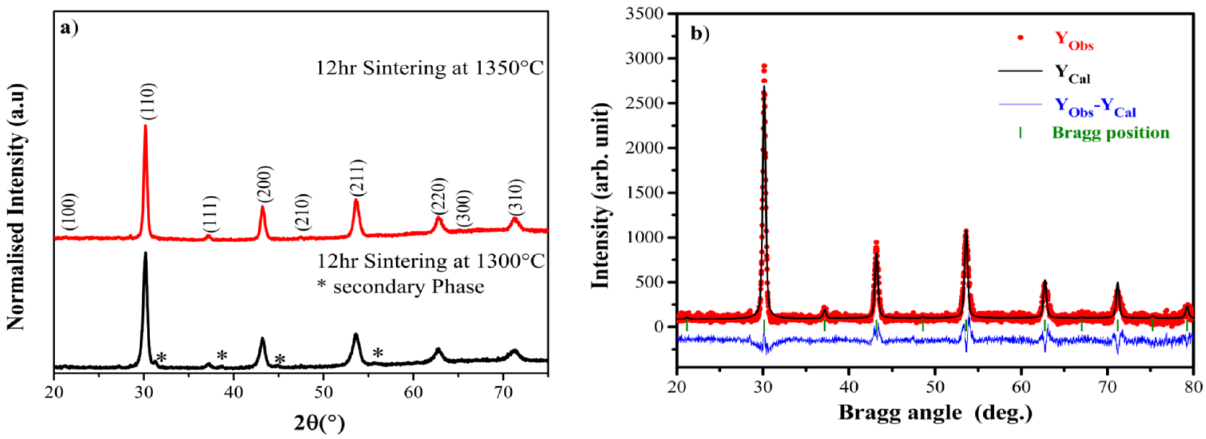

Figure 1. PXRD patterns of the $Ba(Ti_{0.2}Zr_{0.2}Hf_{0.2}Sn_{0.2}Ce_{0.2})O_3$ samples calcined at 1300 and sintered at 1350 °C (a) and Rietveld refinement of the sample sintered at 1350 °C (b)

III. Results and discussion

3.1. Structural analysis

Figure 1a represents XRD patterns of the sample $Ba(Ti_{0.2}Zr_{0.2}Hf_{0.2}Sn_{0.2}Ce_{0.2})O_3$ calcined at 1300 °C and sintered at 1350 °C for 12 h. A small amount of secondary phase was observed in XRD pattern of the sample heated at 1300 °C, but the sample sintered at 1350 °C has a single phase structure. The Rietveld refinement (Fig. 1b) confirms a pure cubic crystal structure with space group *Pm-3m* (No. 221). The Rietveld refinement yielded R_{wp} and R_p values slightly higher than 15%. Several iterative refinements were performed by optimising background, peak profile, lattice parameters, atomic occupancies and microstructural parameters. However, no further significant reduction in *R*-factors was achieved after convergence. The relatively higher values are attributed to the intrinsic structural complexity of the high-entropy oxide system, particularly the random distribution of multiple cations at the B-site, which induces local lattice distortion and micro strain. Such

chemical disorder is difficult to perfectly model within a conventional single-phase refinement approach. Nevertheless, the refined structural parameters are physically reasonable and the calculated pattern shows good agreement with the observed data without any detectable impurity peaks. Other relevant data of the Rietveld refinement are shown below in Table 1.

Figures 2 and 3 present a detailed analysis of the sample's surface morphology, energy-dispersive X-ray (EDX) spectra and elemental mapping. These characterizations collectively provide comprehensive evidence of the material's structural integrity, revealing a homogeneous surface morphology with uniform grain size distribution. The EDX spectra further support the presence of the expected elements, confirming their stoichiometric composition. Additionally, the elemental mapping highlights the consistent presence of these elements across the sample, thereby substantiating the formation of a single, pure and densely packed phase without detectable impurities or phase segregation.

Table 1. Rietveld refinement data of the sample sintered at 1350 °C

Parameters	Corresponding Values
Crystal system	Cubic
$a=b=c$ [Å]	4.18
$\alpha=\beta=\gamma$ [degree]	90°
Space group	*Pm-3m* (221)
R_e	17.18
R_p (Profile) [%]	17.89
R_{wp} (Weighted Profile) [%]	20.32
Goodness of fit (GOF)	1.39

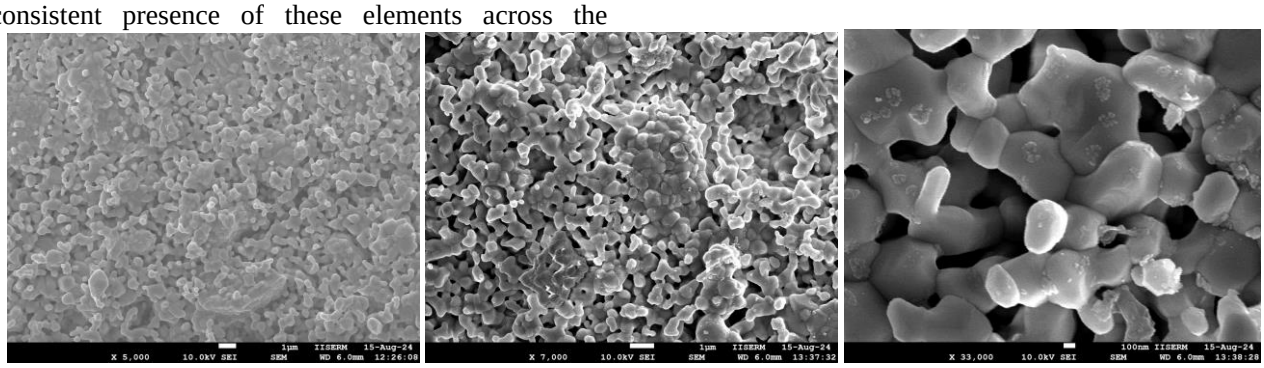

Figure 2. SEM images of the $Ba(Ti_{0.2}Zr_{0.2}Hf_{0.2}Sn_{0.2}Ce_{0.2})O_3$ sample sintered at 1350 °C (at different magnifications)

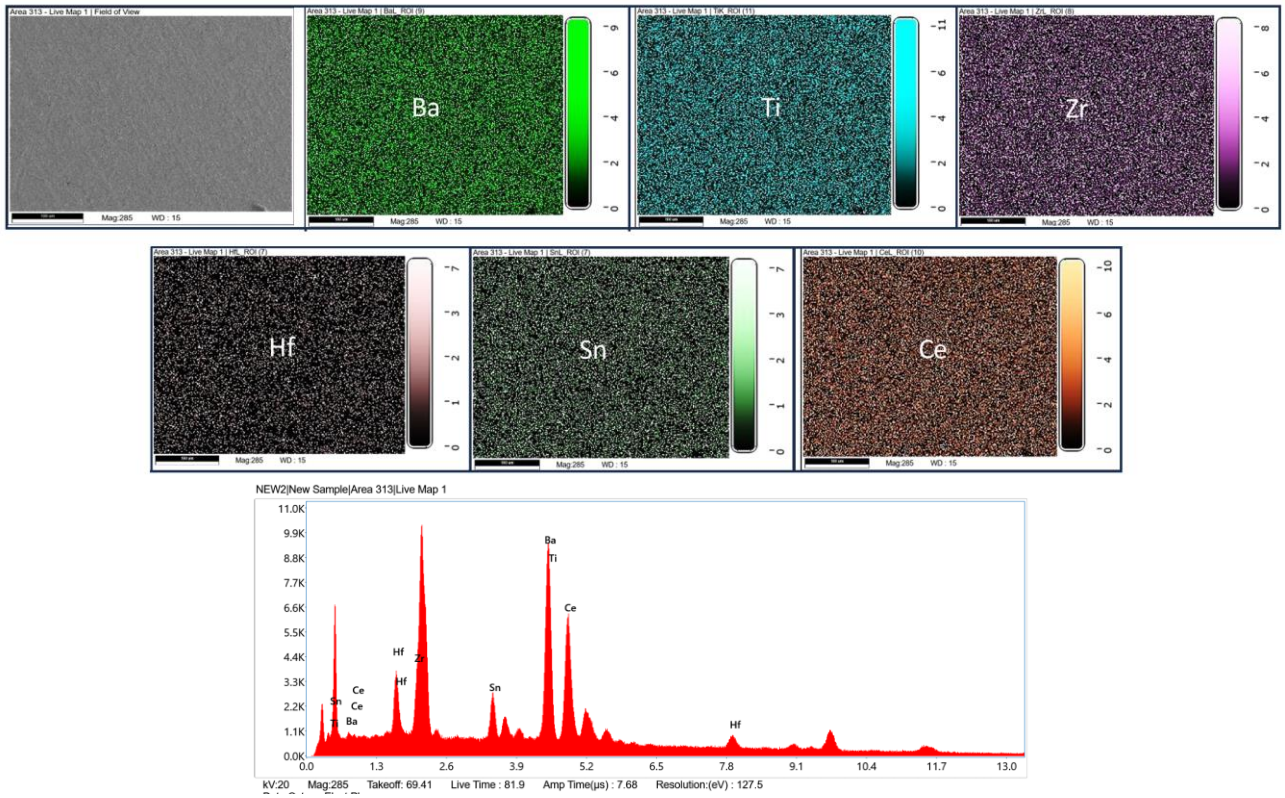

Figure 3. Energy dispersive X-ray spectra (a) and elemental mapping with colour representation (b) of the $Ba(Ti_{0.2}Zr_{0.2}Hf_{0.2}Sn_{0.2}Ce_{0.2})O_3$ sample sintered at 1350 °C

3.2. Impedance spectroscopy

Figure 4 illustrates the variation of the real and imaginary parts of impedance (with frequency across a temperature range of 35 to 495 °C) of the sample sintered at 1350 °C. The real part of impedance decreases with frequency implying relaxation process within the sample. The magnitude of real impedance decreases with temperature at lower frequency range meaning increase in AC conductivity due to the reduction of grain, grain boundaries and electrode-interface resistance. Frequency-independent behaviour of the impedance at higher frequencies can be attributed to the space charge accumulation at the interface between the sample and the electrodes, i.e. release of space charge [25,26]. The imaginary part of the impedance also exhibits a decreasing trend with increasing temperature and frequency. Notably, no relaxation peaks are observed up to 295 °C, indicating a lack of significant dielectric relaxation in this range. Peaks shift towards higher frequencies with increase in temperature due to variation in relaxation process within the material. Also, the asymmetry in the peak indicates electrical conduction process in the sample. This is mainly due to the diffusion of electrons in lower temperature range and defects at higher temperature regime.

Figure 5 highlights a mismatch overlapping pattern between the imaginary parts of the impedance and the electrical modulus, suggesting a nearly short-range ordering of charge carriers within the sample [27,28].

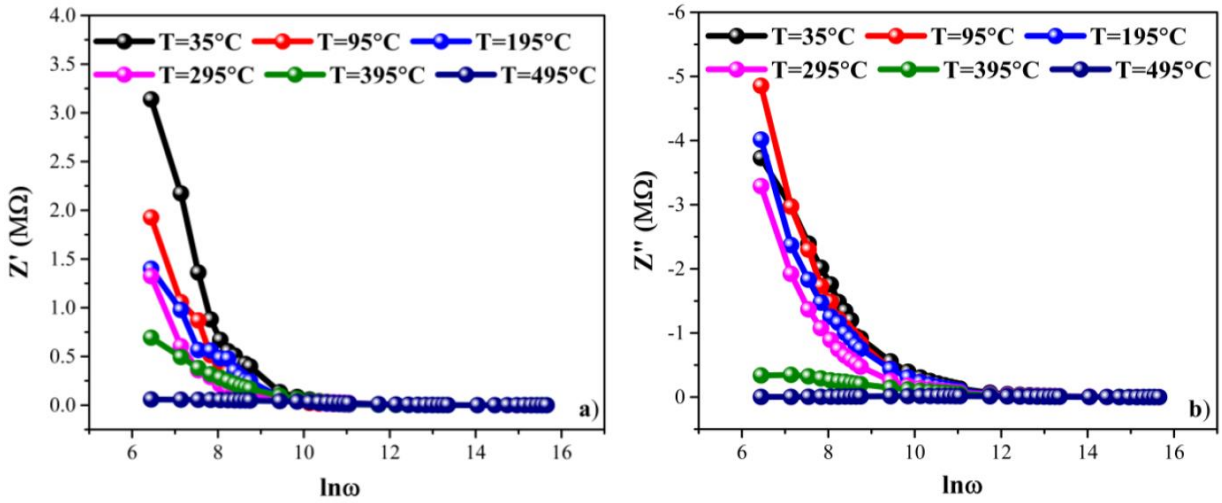

Figure 4. Variation of the real and imaginary components of impedance with frequency across different temperatures

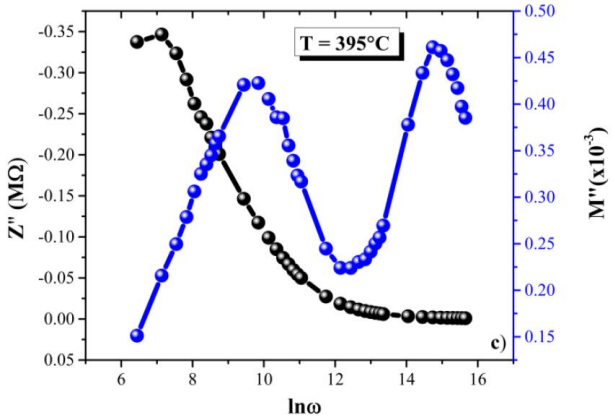

Figure 5. Comparison of imaginary part of impedance and modulus

3.3. AC conductivity

Figure 6 illustrates the temperature-dependent variation of the real and imaginary parts of AC conductivity vs. frequency of the sample sintered at 1350 °C. Conductivity increases by increasing both frequency and temperature. At lower frequencies, a plateau is observed in which AC conductivity is constant and extends towards higher frequency with temperature. At this range of frequencies, the random diffusion of charge carriers via hoping leads to almost temperature independent AC conductivity. Observed behaviour of AC conductivity further confirms the semiconducting nature of the sample, characterised by a negative temperature coefficient of resistance [25,26,29]. This phenomenon can be attributed to the enhanced thermal excitation of charge carriers at elevated temperatures.

3.4. Electrical modulus

Figure 7 illustrates the frequency-dependent behaviour of the electrical modulus. At lower frequencies, the real component of the modulus is relatively small, indicating minimal contribution from electrode polarisation. As the temperature increases, particularly within the lower frequency range, the real part of the modulus approaches zero, suggesting the absence of electrode polarisation effects. Concurrently, the real part of the modulus exhibits a pronounced

decrease with rising temperature, indicative of an enhancement in the material's conductivity. The imaginary component of the modulus displays well defined peaks that progressively shift to higher frequencies with increasing temperature, accompanied by a corresponding increase in peak magnitude. This behaviour is consistent with the relaxation dynamics occurring within the sample. The observed peak asymmetry further suggests a temperature-dependent relaxation mechanism, implying complex charge carrier dynamics within the sample [30].

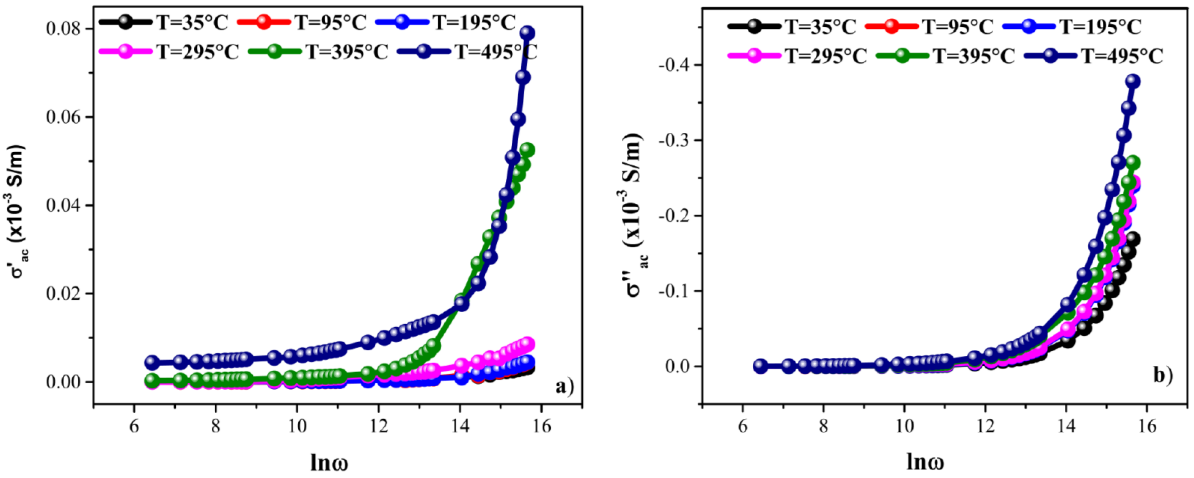

Figure 6. Variation of: a) real and b) imaginary parts of AC conductivity with the natural logarithm of frequency across different temperatures

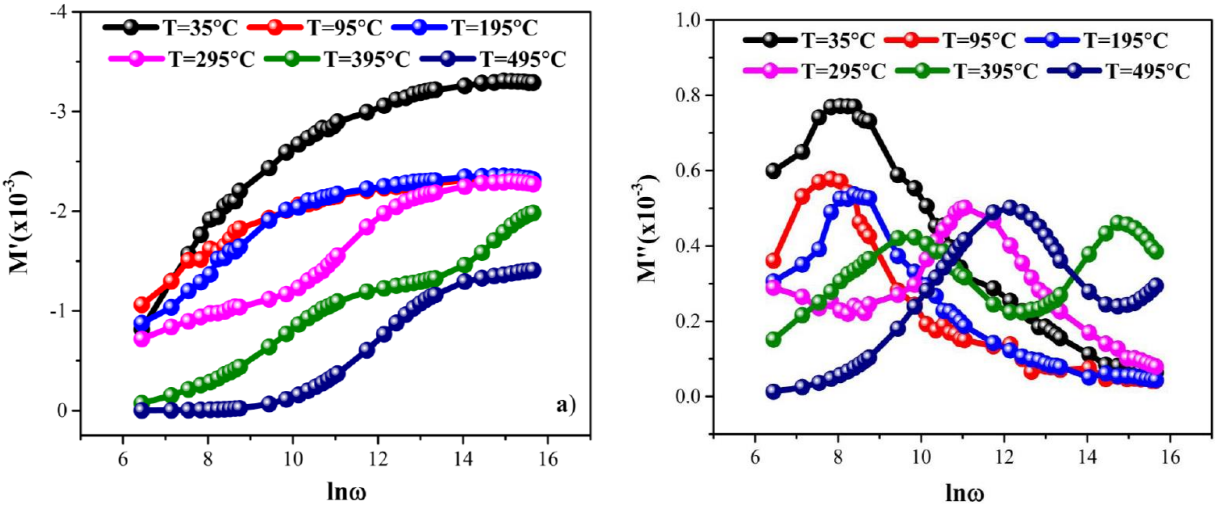

Figure 7. Variation of: a) the real and b) imaginary components of the electrical modulus with the natural logarithm of frequency at various temperatures

3.5. The Nyquist plot

Figure 8 displays the complex impedance plots at various temperatures. The Nyquist plot gives an idea about separation of surface and bulk conduction phenomenon. At lower frequency range it shows the surface effect due to the electrode polarisation which is a highly capacitive phenomenon and characterised by the large relaxation time, whereas the bulk effect occurs at higher frequency range due to interior grain mainly. The gradual decrease in the radius of the semicircles with increasing temperature indicates a reduction in impedance, facilitating greater charge carrier participation in the conduction process. This behaviour highlights the semiconducting nature of the material and demonstrates the role of thermal stimulation in enhancing the conduction mechanism at higher temperatures [31].

IV. Conclusions

A novel high-temperature, high-entropy perovskite, $Ba(Ti_{0.2}Zr_{0.2}Hf_{0.2}Sn_{0.2}Ce_{0.2})O_3$, was successfully synthesised via the traditional solid-state method and finally sintered at 1350 °C for 12 h. Initial characterisations confirmed the formation of a pure polycrystalline cubic phase (*Pm-3m*), as demonstrated

by X-ray diffraction and scanning electron microscopy analyses. Complex impedance spectroscopy reveals the presence of both grain and grain-boundary contributions to the relaxation process of the sintered high-entropy material. Additionally, the significant broadening of the peaks observed in the imaginary components of impedance and electrical modulus suggests temperature-dependent relaxation behaviour within the material. These stable electrical properties of the high-entropy perovskite indicate promising potential for advanced applications in the electronics industry.

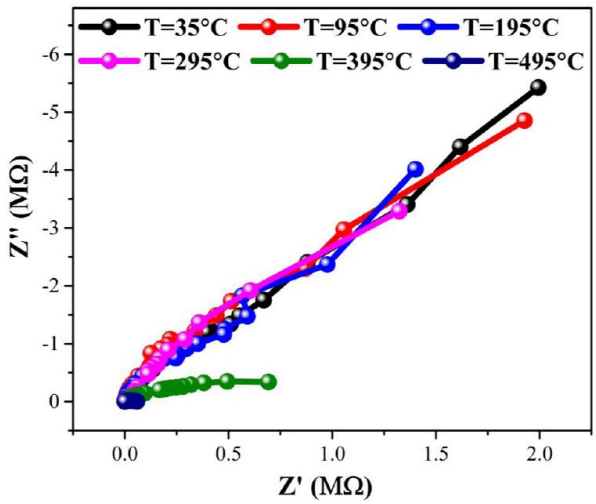

Figure 8. Variations in complex impedance (*Z''* vs. *Z'*) across different temperatures

Acknowledgement: The authors are deeply indebted to St. Xavier's College, Ranchi, India, for its generous financial support. Rupesh Kumar, gratefully acknowledges the Council of Scientific and Industrial Research–University Grants Commission (CSIR-UGC), New Delhi, India, for the award of a Junior Research Fellowship (Ref. No. 211610018034/2022).

References

1. V. Goldschmidt, "Die Gesetze der Krystallochemie", *Naturwissenschaften*, **14** (1926) 477–485.
2. N.J.M.S. Ramadass, "ABO_3-type oxides - Their structure and properties - A bird's eye view", *Mater. Sci. Eng.*, **36** [2] (1978) 231–239.
3. M.S. Wrighton, A.B. Ellis, P.T. Wolczanski, D.L. Morse, H.B. Gray, and D.S. Ginley, "Strontium titanate photoelectrodes. Efficient photoassisted electrolysis of water at zero applied potential", *J. Am. Chem. Soc.*, **98** [10] (1976) 2774–2779.
4. K.F. Wang, J.M. Liu, Z.F. Ren, "Multiferroicity: the coupling between magnetic and polarization orders", *Adv. Phys.*, **58** [4] (2009) 321–448.
5. N.Q. Minh, "Ceramic fuel cells", *J. Am. Ceram. Soc.*, **76** [3] (1993) 563–588.
6. Z. Wang, C. Zhao, H. Wang, M. Wang, C. Liu, D. Yang, Y. Li, "Preparation and irradiation stability of $A_2B_2O_7$ pyrochlore high-entropy ceramic for immobilization of high-level nuclear waste", *J. Nucl. Mater.*, **574** (2023) 154212.
7. Z. Zhao, H. Chen, H. Xu, F.-Z. Du, X. Wang, W. Xu, K. Sun, Z. Peng, Y. Zhang, "$(Y_{0.25}Yb_{0.25}Er_{0.25}Lu_{0.25})_2(Zr_{0.5}Hf_{0.5})_2O_7$: A defective fluorite structured high entropy ceramic with low thermal conductivity and close thermal expansion coefficient to Al_2O_3," *J. Adv. Ceram.*, **9** [3] (2020) 303–317.
8. N. Wang, M. Cao, Z. He, C. Diao, Q. Zhang, Y. Zhang, J. Dai, F. Zeng, H. Hao, Z. Yao, H. Liu, "Structural and dielectric behavior of giant permittivity $SrNb_xTi_{1-x}O_3$ ceramics sintered in nitrogen atmosphere", *Ceram. Int.*, **42** [12] (2016) 13593–13600.
9. P. Yadav, S. Yadav, S. Atri, R. Tomar, "A brief review on key role of perovskite oxides as catalyst", *ChemistrySelect*, **6** [45] (2021) 12947–12959.
10. Z. Fan, K. Sun, J. Wang, "Perovskites for photovoltaics: A combined review of organic–inorganic halide perovskites and ferroelectric oxide perovskites", *J. Mater. Chem. A*, **3** [37] (2015) 18809–18828.
11. A.S. Bhalla, R. Guo, R. Roy, "The perovskite structure - A review of its role in ceramic science and technology", *Mater. Res. Innov.*, **4** [1] (2000) 3–26.
12. A. Zeb, S.J. Milne, "High temperature dielectric permittivity perovskites", *J. Mater. Sci. Mater. Electron.*, **26** (2015) 9243–9255.
13. A.K. Yadav, C. Gautam, "Dielectric behavior of perovskite glass ceramics", *J. Mater. Sci. Mater. Electron.*, **25** (2014) 5165–5187.
14. S.J. Skinner, "Recent advances in perovskite-type materials for solid oxide fuel cell cathodes", *Int. J. Inorg. Mater.*, **3** [2] (2001) 113-121.
15. S.P. Jiang, "Development of lanthanum strontium manganite perovskite cathode materials of solid oxide fuel cells: a review", *J. Mater. Sci.*, **43** [21] (2008) 6799-6833.
16. P. Kaur, K. Singh, "Review of perovskite-structure related cathode materials for solid oxide fuel cells", *Ceram. Int.*, **46** [5] (2020) 5521–5535.
17. Y. Ning, Y. Pu, C. Wu, Z. Chen, X. Zhang, L. Zhang, B. Wang, "Design strategy of high-entropy perovskite energy-storage ceramics: A review", *J. Eur. Ceram. Soc.*, **44** [8] (2024) 4831-4843.
18. A. Amiri, R. Shahbazian-Yassar, "Recent progress of high-entropy materials for energy storage and conversion", *J. Mater. Chem. A*, **9** [2] (2021) 782-823.
19. Y. Ma, Y. Ma, Q. Wang, S. Schweidler, M. Botros, T. Fu, H. Hahn, T. Brezesinski, B. Breitung, "High-entropy energy materials: challenges and new opportunities", *Energy Environ. Sci.*, **14** [5] (2021) 2883-2905.
20. Q. Yang, G. Wang, H. Wu, B.A. Beshiwork, D. Tian, S. Zhu, Y. Yang, X. Lu, Y. Ding, Y. Ling, Y. Chen, B. Lin, "A high-entropy perovskite cathode for solid oxide fuel cells", *J. Alloys Compd.*, **872** (2021) 159633.
21. L. Zhou, F. Li, J.-X. Liu, S.-K. Sun, Y. Liang, G.-J. Zhang, "High-entropy $A_2B_2O_7$-type oxide ceramics: a potential immobilising matrix for high-level radioactive waste", *J. Hazard. Mater.*, **415** (2021) 125596.
22. S. Ye, J. Zhu, S. Zhu, Y. Zhao, M. Li, Z. Huang, H. Wang, J. He, "Design strategies for perovskite-type high-

entropy oxides with applications in optics", *ACS Appl. Mater. Interfaces*, **15** [40] (2023) 47475–47486.
23. Y. Song, S. Lan, B. Yang, Y. Zheng, Z. Zhou, C.-W. Nan, Y.-H. Lin, "High-entropy design for 2D halide perovskite", *J. Am. Chem. Soc.*, **146** [29] (2024) 19748–19755.
24. S. Jiang, T. Hu, J. Goldstein, N. Zhang, J. Ni, M. Qi, T. Hufnagel, K. Vecchio, J. Luo, "A new class of high-entropy perovskite oxides", *Scr. Mater.*, **142** (2018) 116–120.
25. D.K. Mahato, A. Dutta, T.P. Sinha, "Impedance spectroscopy analysis of double perovskite Ho_2NiTiO_6", *J. Mater. Sci.*, **45** (2010) 6757–6762.
26. R. Kumar, D. Eqbal, S.K. Pandey, S.K. Roy, K. Mamta, R.K. Singh, "A novel multi-cation high-entropy ceramic $Sr(Ti_{0.25}Zr_{0.25}Hf_{0.15}Sn_{0.25}Mn_{0.1})O_3$ for advanced functional electronic applications", *ChemistrySelect*, **10** [48] (2025) e05242.
27. S.N. Das, S.K. Pradhan, S. Bhuyan, S. Sahoo, R.N.P. Chaudhary, M.N. Goswami, "Dielectric and impedance characteristics of nickel-modified $BiFeO_3$-$BaTiO_3$ electronic compound", *J. Electron. Mater.*, **47** (2018) 843–854.
28. R. Padhee, P.R. Das, B.N. Parida, R.N.P. Choudhary, "Electrical and pyroelectric properties of lanthanum based niobate", *J. Phys. Chem. Solids*, **74** [2] (2013) 377–385.
29. R. Kumar, R.K. Singh, K. Mamta, S.K. Roy, S.K. Pandey, "Ultra-low thermal conductivity and dielectric stability in novel high-entropy perovskite oxides for advanced thermal and electronic applications", *J. Mater. Sci. Mater. Electron.*, **37** (2026) 264.
30. M. Kumar, S.K. Roy, R.K. Singh, K. Prasad, "Double perovskite Nd_2FeTiO_6 ceramics: Structural and electrical properties", *Process. Appl. Ceram.*, **17** [4] (2023) 428–435.
31. R. Roy and A. Dutta, "Effect of vanadium doping on the electrical charge transport and dielectric relaxation properties of sodium bismuth titanate perovskite", *Ceram. Int.*, **47** [11] (2021) 15732–15742.